

One-dimensional topological superconductivity in a van der Waals heterostructure

Jose Martinez-Castro,^{1,2,3,*†} Tobias Wichmann,^{1,2,4,†} Keda Jin,^{1,2,3} Tomas Samuely,⁵ Zhongkui Lyu,^{1,2,4} Jiaqiang Yan,⁶ Oleksander Onufriienko,⁵ Pavol Szabó,⁵ F. Stefan Tautz,^{1,2,4} Markus Ternes,^{1,2,3} and Felix Lüpke^{1,2}

¹*Peter Grünberg Institut (PGI-3), Forschungszentrum Jülich, 52425 Jülich, Germany*

²*Jülich Aachen Research Alliance, Fundamentals of Future Information Technology, 52425 Jülich, Germany*

³*Institut für Experimentalphysik II B, RWTH Aachen, 52074 Aachen, Germany*

⁴*Institut für Experimentalphysik IV A, RWTH Aachen, 52074 Aachen, Germany.*

⁵*Centre of Low Temperature Physics, Faculty of Science, Pavol Jozef Šafárik University & Institute of Experimental Physics, Slovak Academy of Sciences, 04001 Košice, Slovakia*

⁶*Materials Science and Technology Division, Oak Ridge National Laboratory, Oak Ridge, TN 37831, USA*

[†]These authors contributed equally

*E-mail: j.martinez@fz-juelich.de

One-dimensional (1D) topological superconductivity is a state of matter that is not found in nature. However, it can be realised, for example, by inducing superconductivity into the quantum spin Hall edge state of a two-dimensional topological insulator [1, 2]. Because topological superconductors are proposed to host Majorana zero modes [3–5], they have been suggested as a platform for topological quantum computing [6, 7]. Yet, conclusive proof of 1D topological superconductivity has remained elusive [1, 8–12]. Here, we employ low-temperature scanning tunnelling microscopy to show 1D topological superconductivity in a van der Waals heterostructure by directly probing its superconducting properties, instead of relying on the observation of Majorana zero modes at its boundary [13–16]. We realise this by placing the two-dimensional topological insulator monolayer WTe₂ on the superconductor NbSe₂. We find that the superconducting topological edge state is robust against magnetic fields, a hallmark of its triplet pairing. Its topological protection is underpinned by a lateral self-proximity effect, which is resilient against disorder in the monolayer edge. By creating this exotic state in a van der Waals heterostructure, we provide an adaptable platform for the future realization of Majorana bound states. Finally, our results more generally demonstrate the power of Abrikosov vortices as effective experimental probes for superconductivity in nanostructures.

Intrinsic one-dimensional (1D) superconductivity is unattainable because in one dimension quantum fluctuations suppress long-range order [17]. This fundamental limitation can be overcome by inducing superconductivity via the proximity effect into quasi-1D systems such as nanowires [18], magnetic atomic chains [19], topological boundary states of quantum spin Hall (QSH) insulators [1, 20], or higher-order topological insulators [21]. Topological edge states in van der Waals (vdW) heterostructures are a natural platform to engineer 1D topological superconductivity (TSC), because different materials can be stacked easily and

with atomically clean interfaces. Moreover, the surfaces of vdW heterostructures are accessible to scanning tunnelling microscopy (STM), in contrast to buried quantum well structures. This facilitates local spectroscopy which also has been an effective tool in the search for Majorana states in 2D topological superconductors [16, 22–24]. A prototypical material to realize 1D TSC is monolayer (ML) WTe₂, an intrinsic QSH insulator [25–28]. The spin-polarized edge states in ML WTe₂ show quantized transport [29–31] and behave like a Tomonaga-Luttinger liquid [32], which establishes their one-dimensional metallicity. Although the spectroscopic features of the QSH edge state coexist with an induced superconducting gap in ML WTe₂/NbSe₂ heterostructures [33, 34], this does not yet prove 1D TSC.

Proximity superconductivity in WTe₂/NbSe₂ heterostructures

Our experiments were carried out on a WTe₂/NbSe₂ heterostructure with regions of ML and bilayer (BL) WTe₂ and exposed areas of the supporting ~ 80 nm thick NbSe₂ flake (Fig. 1a, b). It was fabricated by a modified dry-transfer flip technique [33] (Methods section), which ensures that during the stacking neither the surface nor the interface come into contact with polymers or solvents. This approach is crucially important here, because scanning tunnelling spectroscopy (STS) experiments are extremely sensitive to the inevitable contamination caused by such contacts.

The evolution of the superconducting pairing gap Δ as a function of WTe₂ thickness shows a step-wise shrinking (Fig. 1c, d), which is in line with previous reports [33, 34]. It indicates the expected weakening of the proximity-induced superconductivity in the WTe₂. However, at the ML WTe₂/NbSe₂ step we observe an additional constriction of the gap (Fig. 1d) on the upper terrace next to the edge of the topologically nontrivial ML WTe₂—at precisely the position of the QSH edge state, known to occur on top of the step edge [26, 27, 33–35]. A similar but weaker constriction is also seen at the BL WTe₂/ML WTe₂ step. In this case it occurs be-

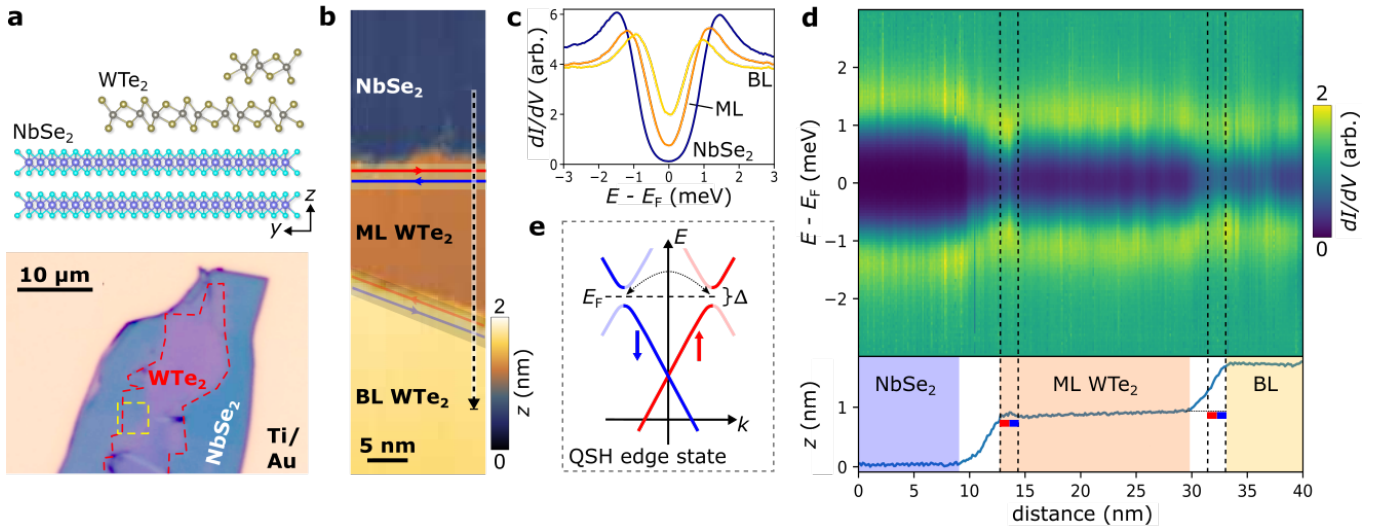


FIG. 1. **Proximity-induced superconductivity in a WTe₂/NbSe₂ heterostructure.** (a) Cross-sectional atomic structure model (top) and optical micrograph (bottom) of the heterostructure. The outline of the WTe₂ flake is indicated by a dashed red line, the investigated area by a yellow dashed line. (b) STM topography of the WTe₂ flake edge. The QSH edge state around the monolayer (ML) region is indicated by red and blue arrows. (c) dI/dV spectra of NbSe₂, monolayer (ML) and bilayer (BL) WTe₂, each showing the respective superconducting pairing gap ($T_{\text{eff}} \approx 2$ K). (d) Spectral map (top) taken along the dashed arrow in panel b and corresponding topography cross section (bottom) with QSH edge states indicated in red and blue. Edge state regions are marked by dashed black lines in the spectral map. (e) Schematic of the ML WTe₂ QSH edge state band structure. Inducing a superconducting pairing gap Δ at the Fermi energy E_F gives rise to an effective 1D p -wave superconductor. Faint lines indicate the particle-hole symmetric spectrum.

low the trivial BL WTe₂ terrace (Fig. 1d), i.e., again at the expected position of the QSH edge state [35]. In contrast, such a constriction is not observed at the BL WTe₂/NbSe₂ step (Extended Data Fig. 1). At both step edges of the ML WTe₂ region we thus observe induced pairing gaps Δ that differ from the one on the adjacent 2D terrace. This points to an intrinsically different pairing mechanism in the QSH edge state. In the following, we will focus on the edge state at the ML WTe₂/NbSe₂ boundary, since it is easier to access by the STM tip [35].

Caroli-de Gennes-Matricon states

Next, we apply an external magnetic field perpendicular to the surface to induce Abrikosov flux vortices in the heterostructure. By carefully tuning the magnetic field, we can position vortices in various regions of interest, with Fig. 2 displaying two representative situations: a vortex located in the bare NbSe₂ and just intersecting the step edge (Fig. 2a-c), and a vortex located entirely in the ML WTe₂ (Fig. 2d-f). The properties of a vortex in the bare NbSe₂ are revealed by a horizontal cut along arrow I in Fig. 2b. Coming from outside the vortex, we observe the expected gradual closing of the pairing gap, with a peak at the Fermi energy emerging in the vortex centre (Fig. 2c) [36]. This well-known feature derives from Caroli-de Gennes-Matricon (CdGM) states [37]. They are bound quasiparticles of energy $E = \pm\mu\Delta^2/E_F$, where $\mu = (\frac{1}{2}, \frac{3}{2}, \dots)$ is the orbital angular momentum and Δ the in-

trinsic pairing gap in the absence of magnetic field. The bound states appear in the confinement potential for normal electrons that is created by the linearly vanishing superconducting energy gap close to the vortex core. Because in NbSe₂ the ratio Δ^2/E_F is very small, we observe a single peak centered at zero bias instead of a series of states for different values of μ [38]. For the vortex in the proximitized ML WTe₂ (Fig. 2d-f), the same qualitative picture emerges as for the vortex in the NbSe₂, as revealed by in Fig. 2e, f (see also Extended Data Fig. 2). Quantitative differences are readily explained by the fact that in STM we now observe the CdGM states in the ML WTe₂, where the induced pairing gap Δ , and therefore ϵ , is smaller than in the bare NbSe₂.

Coming back to the vortex intersecting the ML WTe₂ edge (Fig. 2a), spectra taken along arrow III in Fig. 2b elucidate the interaction of the flux vortex in the NbSe₂ with the proximitized WTe₂ and its QSH edge state. Remarkably, we observe an extremely sharp transition in which the dI/dV spectrum changes from a fully developed CdGM peak in NbSe₂ to a well-formed superconducting gap in the ML WTe₂ edge state (Fig. 2g, h). This occurs from one pixel to the next, corresponding to a lateral distance of less than 10 Å, while on the opposite side, in the NbSe₂, the transition from peak to gap is gradual as expected (Fig. 2g, h). The gapped spectrum in ML WTe₂ demonstrates the absence of CdGM states and thus also the lack of any appreciable ring current there. However, in the NbSe₂ the ring current must extend below the ML WTe₂, because flux vortices are always fully encircled by a ring current with a total phase accumulation of 2π . We can thus conclude

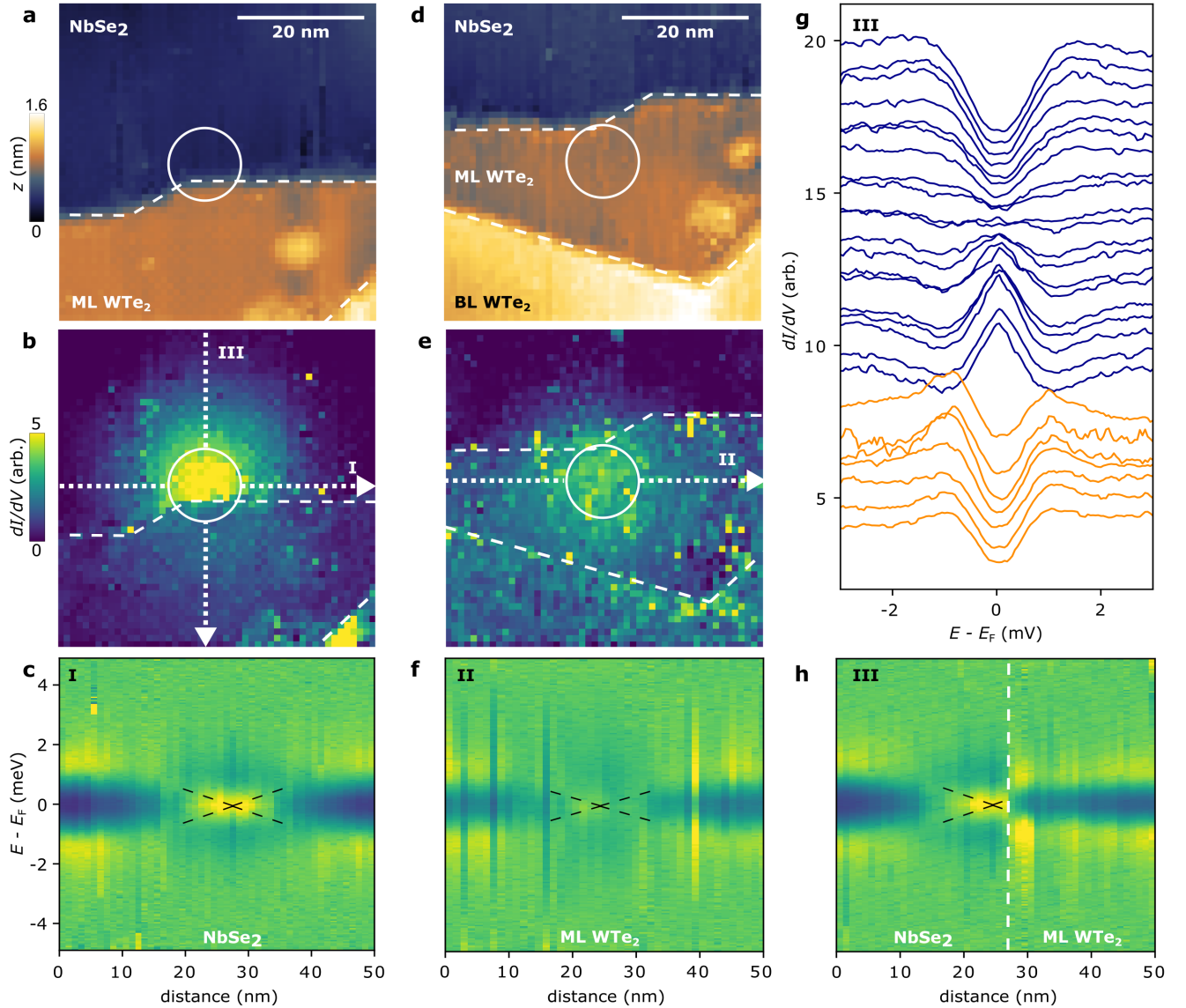


FIG. 2. Influence of an Abrikosov vortex on the induced superconductivity in monolayer WTe₂. (a) STM topography of the ML WTe₂ edge next to which a flux vortex, indicated by the white circle, was positioned ($B_{\text{ext}} = 328$ mT). (b) dI/dV map at zero bias voltage in the same scan frame as panel a, showing the flux vortex in the NbSe₂ as an area of strongly increased tunnelling conductance inside the white circle. The edges of the ML WTe₂ region are indicated by white dashed lines in panels a and b. (c) dI/dV spectral map recorded along arrow I parallel to the ML WTe₂ edge and across the flux vortex in panel b. (d) Topography of the ML WTe₂ terrace on which an Abrikosov vortex was placed at the position indicated by the white circle ($B_{\text{ext}} = 450$ mT). (e) dI/dV map at zero bias voltage in the same scan frame as panel d, showing the flux vortex as an area of slightly increased tunnelling conductance inside the white circle. The edges of the ML and BL WTe₂ regions are indicated by white dashed lines in panels d and e. (f) dI/dV spectral map recorded along arrow II across the vortex in panel e. (g) Waterfall plot of dI/dV spectra recorded along arrow III across the ML WTe₂ step in panel b, showing an abrupt change of the spectral shape from a fully gapped spectrum on the ML WTe₂ (orange curves) to a peak in the NbSe₂ due to CdGM states (blue curves). Curves are offset by 0.5 with respect to each other. (h) dI/dV spectral map recorded along arrow III in panel b. The black dashed lines in panels c, f, and h signify the approximately linear decrease of the superconducting pairing gap towards the centre of the vortex.

that in this configuration the vortex does not extend into the ML WTe₂, in contrast to the situation in Fig. 2d-f.

Probing the edge-state superconductivity

The special experimental situation where a flux vortex is extending below the edge of the ML WTe₂ can be employed to probe how the two-dimensional WTe₂ and its one-

dimensional QSH edge state respond to the laterally varying NbSe₂ pairing gap underneath and the laterally varying penetrating magnetic field. To evaluate the local strength of the superconductivity across the surface, we analyse the relative depth of the pairing gap, defined by

$$\delta_{\text{rel}} \equiv \frac{dI/dV(3\text{ mV}) - dI/dV(0\text{ mV})}{dI/dV(3\text{ mV})}. \quad (1)$$

A value $0 < \delta_{\text{rel}} < 1$ indicates a superconducting gap (with $\delta_{\text{rel}} = 1$ indicating a fully developed gap), while $\delta_{\text{rel}} < 0$ indicates the presence of a peak at zero bias (such as stemming from CdGM states). Although $\delta_{\text{rel}} > 0$ quantifies the relative *depth* of the pairing gap, it also correlates well with the *width* of the gap, as is evident in Fig. 1c.

Plotting δ_{rel} at $B_{\text{ext}} = 0$ along a line across the ML WTe₂ edge (dotted arrow in Fig. 1b) reveals a reduction of approximately 12% (null hypothesis probability $p < 0.005$, see Methods) in the QSH edge state compared to the 2D interior of the ML WTe₂ (blue curve in the top panel of Fig. 3a), in full agreement with the observations discussed in the context of Fig. 1d. Remarkably, in the presence of the vortex in Fig. 2a, b this situation is reversed. Now, the superconductivity in the QSH edge state is locally the strongest, as the red curve in the top panel of Fig. 3a demonstrates: Starting from the NbSe₂, δ_{rel} decreases towards the centre of the vortex, becoming negative in its core (CdGM states) before rapidly increasing back to positive values at the ML WTe₂/NbSe₂ step edge—this is connected to the abrupt change in spectral shape as observed in Fig. 2g—and reaching a local maximum in the QSH edge state. Beyond the QSH edge state, δ_{rel} decreases in the ML WTe₂, before finally rising again. Thus, in a region that is about 3 nm wide, δ_{rel} is *locally increased* by approximately 18% ($p < 0.004$) over the extrapolated behavior of the ML WTe₂ (dashed red line in the top panel of Fig. 3a). This region coincides with the region of *locally decreased* δ_{rel} in the absence of a magnetic field which marks the QSH edge state.

Analysing the energy positions of the superconducting coherence peaks E_{coh} (Fig. 3a, middle panel) with a feature-detection scanning tunnelling spectroscopy (FD-STs) algorithm (Methods and Refs. [39, 40]) supports the observation of a distinct behaviour of the QSH edge state: When the vortex is absent, the coherence peaks in the edge state are approximately 10% closer to E_{F} ($p < 0.003$) than in the ML WTe₂ (Fig. 3a, middle panel, blue curve). When the vortex is present, the situation is not as clear, as, due to the weak intensities of the coherence peaks, their exact energy is more difficult to determine. Nevertheless, we observe a trend to higher E_{coh} , i.e. larger gap sizes, in the region of the QSH edge state (Fig. 3a, middle panel, red curve).

Taking all the evidence together, we conclude that the superconductivity in the QSH edge state at zero magnetic field is weaker than in its 2D surrounding, but at the same time more robust against the presence of the flux vortex underneath and its locally increased magnetic field. Clearly, these distinctive properties indicate an unconventional type of superconductivity, different from the one in the 2D interior of the ML WTe₂.

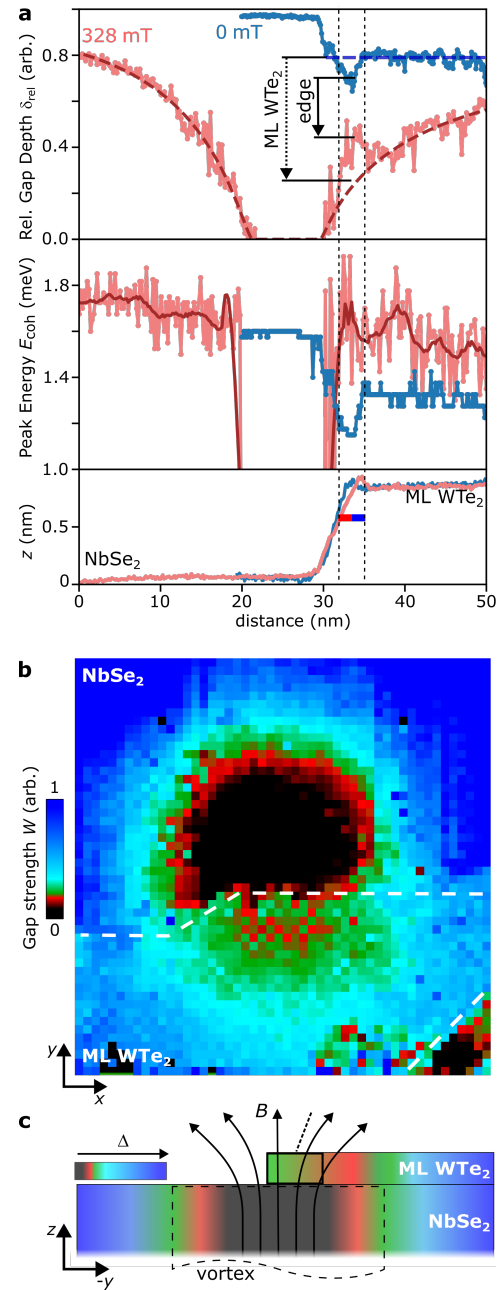


FIG. 3. Robustness of the superconducting QSH edge state. (a) Top panel: Relative depth δ_{rel} of the pairing gap, evaluated along a line across the ML WTe₂/NbSe₂ step edge, with (red) and without (blue) vortex. Blue and red dashed lines describe a constant (0 mT) and a log-normal distribution (328 mT), respectively. Vertical arrows indicate the weakening of δ_{rel} by the vortex, for the ML WTe₂ and QSH edge state, respectively. Middle panel: FD-STs of the coherence peak energy E_{coh} along the same line. Bottom panel: Corresponding topography cross section. Red and blue symbols and the vertical dashed lines indicate the location of the QSH edge state. δ_{rel} and E_{coh} are calculated from the data shown in Fig. 1d and Extended Data Fig. 3. (b) Colour map of the gap strength W at $V = 0$, determined by FD-STs (Methods), in the same scan frame as Fig. 2a, showing a channel of stronger superconductivity along the WTe₂ step edge. The edges of the ML WTe₂ region are indicated by white dashed lines. (c) Schematic vertical cross section through the vortex in panel b. The vortex, indicated by the dashed black line, threads the NbSe₂ flake and extends under the ML WTe₂ and its QSH edge state, the latter outlined by a black box, but in this configuration does not thread the ML WTe₂. Arrows indicate the magnetic field penetrating the flux vortex and WTe₂. The colour scale represents the pairing gap Δ .

Since an enhanced robustness against magnetic fields is a hallmark of the triplet-like pairing in the spin-momentum-locked QSH edge state, our data therefore provide direct experimental proof for 1D TSC in the proximitized QSH edge state.

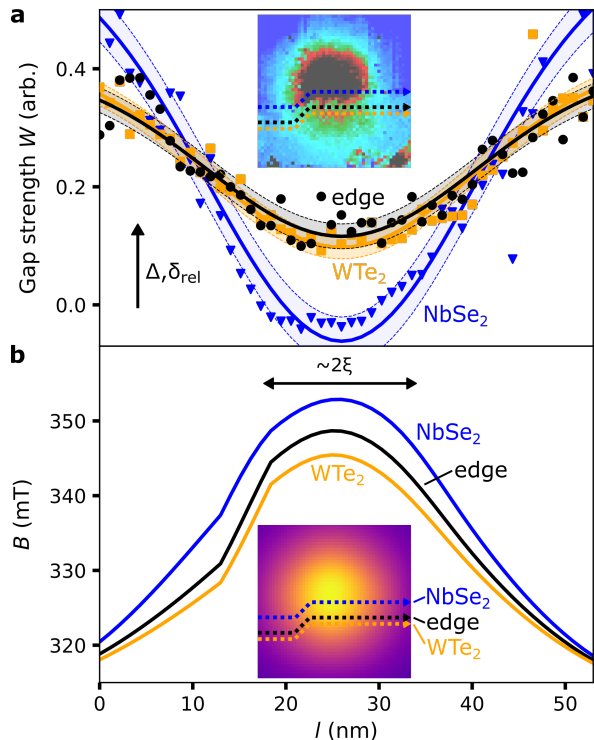


FIG. 4. Lateral proximity effect in the QSH edge state. (a) FD-STs gap strength W as function of distance l along three paths parallel to the step edge, directly at the position of the edge (black circles), inside the ML WTe₂ (orange squares, 2 nm from the step edge) and on the NbSe₂ (blue triangles, 5 nm from the step edge). The solid lines are Gaussian fits to the data points, with dashed lines and shaded areas marking 1σ confidence intervals, respectively (Methods). The black arrow indicates the direction of increasing pairing gap Δ and relative gap depth δ_{rel} . Inset: FD-STs map from Fig. 3b, with colour-coded paths. (b) Calculated magnetic field of the NbSe₂ flux vortex, plotted along the three paths defined in panel a. Note the different order of ML WTe₂ (orange curves) and QSH edge state (black curves) in the calculated magnetic fields and the FD-STs intensities, respectively. Inset: Map of the magnetic field with indicated paths.

Lateral self-proximity effect in the 1D topological superconductor

Having demonstrated the side-by-side coexistence of different types of superconductivity in the heterostructure, we now analyse their lateral and vertical interactions. For this purpose, we use the FD-STs algorithm to extract the steepness of the superconducting gap W (Methods), which scales with both δ_{rel} and E_{coh} , but is a more sensitive measure of the gap strength. Extracting W from the dI/dV map in Fig. 2b again

reveals the sharp truncation of the vortex's signature at the step edge (Fig. 3b). However, in contrast to the dI/dV map, the W map shows a vortex-related structure on the ML WTe₂ (green and red circle segments in Fig. 3b), which agrees well with the single line-cut of δ_{rel} in Fig. 3a. This structure must stem from the interaction of the ML WTe₂ with the vortex in the NbSe₂, which extends seamlessly underneath the WTe₂ flake (see above).

Remarkably, within the region of the ML WTe₂ in Fig. 3b that is affected by the vortex, the red segment is separated from the step edge by a green channel. This channel of enhanced superconductivity close to the vortex core precisely tracks the QSH edge state, also following the kink in the step edge. It is important to note that, since the proximity effect from NbSe₂ acts vertically, the gap distribution in the proximitized ML WTe₂ should in principle directly correlate with the pairing gap in the underlying NbSe₂. Since this is not the case here, we suggest the existence of a lateral self-proximity effect.

To analyse this effect in detail, we plot the gap strength W along three parallel paths, one tracing the QSH edge state, the other two offset by 5 nm into the NbSe₂ and 2 nm into the ML WTe₂ (Fig. 4a). Using the coherence length ξ and penetration depth λ of NbSe₂, we calculate the magnetic field in the NbSe₂ vortex along these paths (Fig. 4b, Methods). While the penetrating field in the centre of the vortex reaches a maximum of $B \sim 352$ mT, the field is smaller in the QSH edge state and the ML WTe₂, because they are further away from the vortex core. At the same time Fig. 4a reveals that the QSH edge state as well as the ML WTe₂ exhibit superconductivity that does not reflect the vanishing gap in the NbSe₂ below. Because the ML WTe₂ and its QSH edge state are not intrinsically superconducting and the vertical proximity effect essentially drops out as origin of their superconductivity, lateral self-proximity effects from outside the vortex within both must therefore be at play. Yet, despite the higher field in the QSH edge state we observe a significantly stronger superconductivity there ($p < 0.17$) than in the ML WTe₂ (black vs. orange curves in Fig. 4a). This again points to distinct superconductivities in the ML WTe₂ and QSH edge state, respectively. Notably, the lateral self-proximity effect in the QSH edge state is approximately twice as strong as in the ML WTe₂: In the absence of the QSH edge state, δ_{rel} at the edge of the ML WTe₂ would be $\sim 75\%$ smaller than without flux vortex (dotted arrow in Fig. 3a). In contrast, for the edge state the reduction in the presence of the vortex is only $\sim 30\%$ (solid arrow in Fig. 3a). We explain this with the topological protection in the QSH edge state.

For the lateral self-proximity effect to work effectively, the mean free path in the QSH edge state must be equal or larger than the radius of the Abrikosov vortex ($\sim 2\xi \approx 15$ nm). It should be noted, however, that even in the presence of the lateral self-proximity effect, the Cooper pairs in the QSH edge state are exposed to the penetrating magnetic field from the vortex underneath, which leads to a local weakening of the pairing gap in the QSH edge state as the vortex is crossed.

This can clearly be observed in Fig. 4a.

In conclusion, we demonstrated that individual Abrikosov flux vortices can be used to probe superconducting properties locally, on length scales substantially below the vortex diameter. With this approach we showed that the QSH edge state of ML WTe₂ is topologically superconducting, exhibiting a notable robustness against local magnetic fields and kinks in the edge, as well as a strong lateral proximity effect. We anticipate that our result marks a crucial step towards the engineering of Majorana bound states based on QSH insulators [4].

METHODS

Sample fabrication

WTe₂ and NbSe₂ were exfoliated onto 285 nm SiO₂/Si substrates and were assembled into heterostructures using a modified dry-transfer flip technique [33]. In short, the flakes were picked up in reverse order, the heterostructure was then flipped upside down and placed onto pre-evaporated Ti/Au leads on a separate substrate, which was subsequently mounted to a standard STM sample plate. Samples were fabricated in an argon-filled glovebox and transferred to the STM chamber using an ultra-high vacuum suitcase ($p \sim 10^{-10}$ mbar), i.e., without any exposure to air.

Scanning tunnelling microscopy/spectroscopy

Scanning tunnelling data were acquired at the Centre of Low Temperature Physics in Košice in ultra-high vacuum at a base pressure of $p < 10^{-10}$ mbar and a base temperature of 1.14 K using a mechanically cut Au tip. The set point parameters were $V = 5$ mV, $I = 300$ pA for all STM/STS measurements, except those reported in Fig. 1b, which was recorded at $V = 472$ mV, $I = 20$ pA. Tunnelling spectra were acquired using standard lock-in techniques at $f = 789$ Hz and $V_{\text{mod}} = 100$ μ V. The dI/dV maps in Fig. 2a, b, d, e are recorded in 50×50 arrays, over areas of $50 \text{ nm} \times 50 \text{ nm}$.

The effective electronic temperature of the tunnelling junction was $T_{\text{eff}} = 2.16$ K, as determined by fitting the superconducting gap of NbSe₂. Despite recent evidence for a spatial superconducting gap anisotropy of NbSe₂ [41], we used a simplified isotropic two-gap model, which is sufficient for our purposes. Here the density of states is given by

$$N_{2g}(E, \Delta_1, \Delta_2) = CN(E, \Delta_1) + (1 - C)N(E, \Delta_2), \quad (2)$$

with the density of states

$$N(E, \Delta) = N_0 \Re \left[\frac{E}{\sqrt{E^2 - \Delta^2}} \right] \quad (3)$$

from standard BCS theory, where Δ is the superconducting gap and N_0 the normal density of states. To extract the effective tip temperature T_{eff} , the finite temperature differential

conductance is derived as the convolution of the BCS density of states with the derivative of the Fermi function,

$$\frac{dI}{dV}(eV) \propto \int_{-\infty}^{\infty} dE \frac{e^{\frac{E-eV}{k_B T_{\text{eff}}}}}{[e^{\frac{E-eV}{k_B T_{\text{eff}}}} + 1]^2} N_{2g}(E, \Delta_1, \Delta_2). \quad (4)$$

We fitted this function to the NbSe₂ data by varying Δ_1 , Δ_2 , C and T_{eff} . The resulting gap values ($\Delta_1 = 1.36$ meV and $\Delta_2 = 1.0$ meV) are in agreement with the literature [34]. We have applied the same model to extract the superconducting gaps in the WTe₂ spectra, where we fixed T_{eff} to the value obtained from fitting NbSe₂ and only varied Δ_1 , Δ_2 and C . The resulting curves and parameters are displayed in Extended Data Fig. 5a-c.

Feature detection-scanning tunnelling spectroscopy

FD-STs was employed for an unbiased detection of peaks and dips in the dI/dV spectra [39, 40]. Specifically, we applied FD-STs to detect the dips of the superconducting gaps and the peaks of the CdGM states or the coherence peaks. The method is visualized in Extended Data Fig. 4 and works as follows: (1) In a first step, the intrinsic noise in each of the dI/dV spectra was smoothed out with a Savitzky-Golay filter. To avoid filtering out meaningful signal, we used a sliding window of 350 μ V. The Savitzky-Golay filter does not only provide the smoothed dI/dV , but also the smoothed second derivative d^2I/dV^2 . (2) Next, we identified peaks and dips by finding zero crossings in d^2I/dV^2 . (3) We then assigned a weight W to the feature detected in this way by determining the directed difference between each feature's two next-lying extremal values of d^2I/dV^2 , where peaks yield $W > 0$, dips $W < 0$ (Extended Data Fig. 4c). When FD-STs is applied to the superconducting gap, W quantifies the steepness of the gap and is therefore referred to as gap strength W in the main text. Similarly, application to the coherence peaks leads to the coherence peak strength W . (4) Finally, the weights W of the features were plotted as a map. Features for which the algorithm did not return a result were set to zero. This concerns only a few data points on NbSe₂, where CdGM states result in d^2I/dV^2 being too noisy.

We validated the FD-STs map of the superconducting gap strength W in Fig. 3b by comparing it to the relative depth δ_{rel} as defined in Eq. 1. Plotting the FD-STs gap strength W along the same lines as δ_{rel} in Fig. 3a, we find an almost identical behaviour, as shown in Extended Data Fig. 6a. Moreover, the FD-STs map in Extended Data Fig. 6b, which was generated from the energies of the coherence peaks, shows essentially the same behaviour as the FD-STs map of the superconducting gap strength W in Fig. 3b.

The Gaussian fits to line FD-STs line profiles displayed in Fig. 4a are given by the equation

$$y = A \cdot \exp\left(-\frac{(l - l_0)^2}{2\sigma^2}\right) + B, \quad (5)$$

where l_0 was fixed to the centre of the vortex and $\sigma = 2\xi$. Parameters A and B were used to fit the data points.

Vortex calculations

Following Ref. [42], the magnetic field around a single vortex was calculated in radial coordinates as

$$B(r) = \frac{\Phi_0}{2\pi\lambda^2} K_0\left(\frac{r}{\lambda}\right), \quad (6)$$

where K_0 is the zeroth-order modified Bessel function of the second kind, and Φ_0 is the flux quantum. Inside the vortex ($r \lesssim \xi$), the field was approximated by

$$B(0) = \frac{\Phi_0}{2\pi\lambda^2} \ln\left(\frac{\lambda}{\xi}\right). \quad (7)$$

We used $\lambda = 69$ nm as the penetration depth and $\xi = 7.7$ nm as the coherence length of NbSe₂ [43]. To get a continuous distribution of the B field, we interpolated between the two solutions (Eqs. 6 and 7) using a two-dimensional spline with a smoothing factor, which approximately corresponds to a gliding average with window size $\sim \xi$. To simulate our experiments, we constructed a discrete triangular vortex lattice with a density corresponding to the flux density of the externally applied magnetic field ($a = 1.075\sqrt{\Phi_0/B} \approx 85$ nm, which corresponds to an intermediate flux density [42]). The fields penetrating the individual vortices are then added up and evaluated around a single vortex in the centre of the lattice (inset in Fig. 4b).

Statistical analysis

To determine the statistical significance of the data measured at the edge of the ML WTe₂ (data in Fig. 3a) we performed a Student's t -test against the null hypothesis [44]. For this, we determined the standard deviation of the data without the edge signal from the regression curve assuming a normal (Gaussian) distribution. To avoid underestimating the probability p that the observed edge signal is due to random noise, we calculated p using the cumulative Student's t distribution function, which not only takes into account the signal's distance from the regression curve in units of σ , but also the relatively small sample size of only $n = 10$ to 15 data points, for which the Gauss error function would underestimate p . Using the cumulative Student's t distribution, we find small p values which confirm our claims.

ACKNOWLEDGEMENTS

The authors acknowledge helpful discussions with Samir Lounis and thank Francois C. Bocquet for technical support. Furthermore, we are grateful to the Helmholtz Nano Facility for its support regarding sample fabrication. The

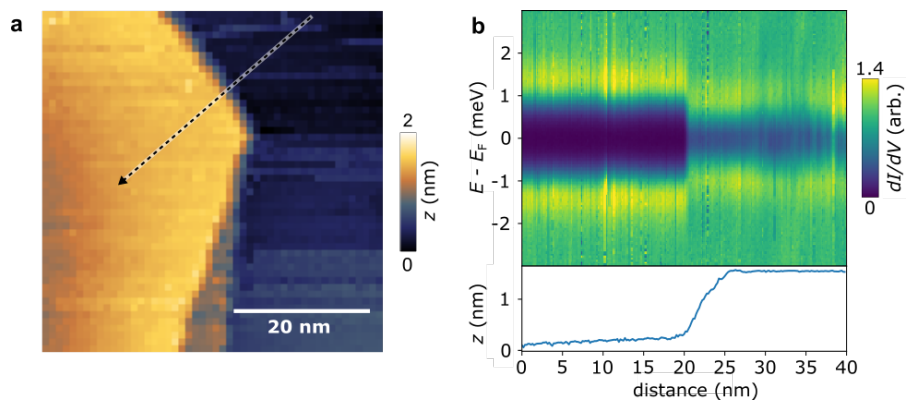
authors acknowledge funding from the European Union's Horizon 2020 Research and Innovation Programme under Grant Agreement no 824109 (European Microkelvin Platform). J.M.C., T.W., K.J., M.T. and F.L. acknowledge funding by the Deutsche Forschungsgemeinschaft (DFG, German Research Foundation) within the Priority Programme SPP 2244 (project nos. 443416235 and 422707584). J.M.C., Z.L., F.S.T. and F.L. acknowledge funding from the Bavarian Ministry of Economic Affairs, Regional Development and Energy within Bavaria's High-Tech Agenda Project "Bausteine für das Quantencomputing auf Basis topologischer Materialien mit experimentellen und theoretischen Ansätzen". J.M.C. acknowledges funding from the Alexander von Humboldt Foundation. T.S., P.S. and O.O. acknowledge the support of APVV-20-0425, VEGA 2/0058/20, Slovak Academy of Sciences project IMPULZ IM-2021-42, COST action CA21144 (SUPERQUMAP) and EU ERDF (European regional development fund) Grant No. VA SR ITMS2014+ 313011W856. M.T. acknowledges support from the Heisenberg Program (Grant No. TE 833/2-1) of the German Research Foundation. F.L. acknowledges financial support by Germany's Excellence Strategy - Cluster of Excellence Matter and Light for Quantum Computing (ML4Q) through an Independence Grant. J.Q.Y. was supported by the US Department of Energy, Office of Science, Basic Energy Sciences, Materials Sciences and Engineering Division.

Author contributions. J.M.C., F.S.T., M.T. and F.L. conceived the research. J.M.C., T.W. and F.L. designed the experiments. J.Y. grew WTe₂ crystals. J.M.C., T.W., K.J. and Z.L. fabricated the samples. T.S., O.O. and P.S. set up and provided the STM. J.M.C. and T.W. acquired the data. J.M.C., T.W., F.S.T., M.T. and F.L. analyzed the data. J.M.C., T.W., P.S., M.T., F.S.T. and F.L. developed the physical interpretation. J.M.C., T.W., F.S.T. and F.L. wrote the paper. All authors commented on the manuscript. J.M.C., F.S.T., M.T. and F.L. supervised the research.

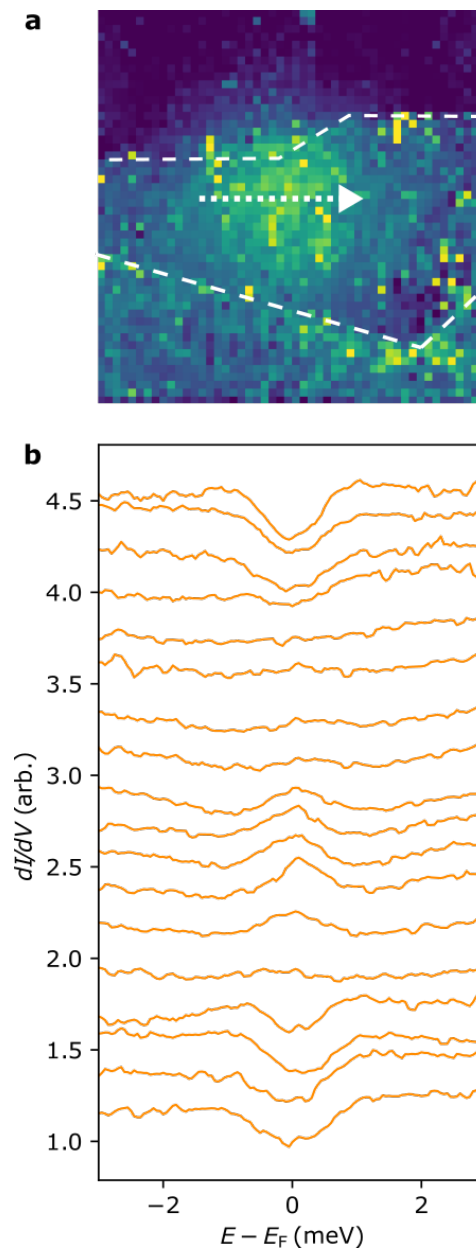
Competing financial interests. The authors declare no competing financial interests.

-
- [1] Bocquillon, E. *et al.* Gapless Andreev bound states in the quantum spin Hall insulator HgTe. *Nat. Nanotechnol.* **12**, 137 (2016).
 - [2] Jäck, B. *et al.* Observation of a Majorana zero mode in a topologically protected edge channel. *Science* **364**, 1255–1259 (2019).
 - [3] Kitaev, A. Y. Unpaired Majorana fermions in quantum wires. *Phys.-Usp.* **44**, 131–136 (2001).
 - [4] Alicea, J. New directions in the pursuit of majorana fermions in solid state systems. *Rep. Prog. Phys.* **75**, 076501 (2012).
 - [5] Flensberg, K., von Oppen, F. & Stern, A. Engineered platforms for topological superconductivity and Majorana zero modes. *Nat. Rev. Mater.* **6**, 944–958 (2021).

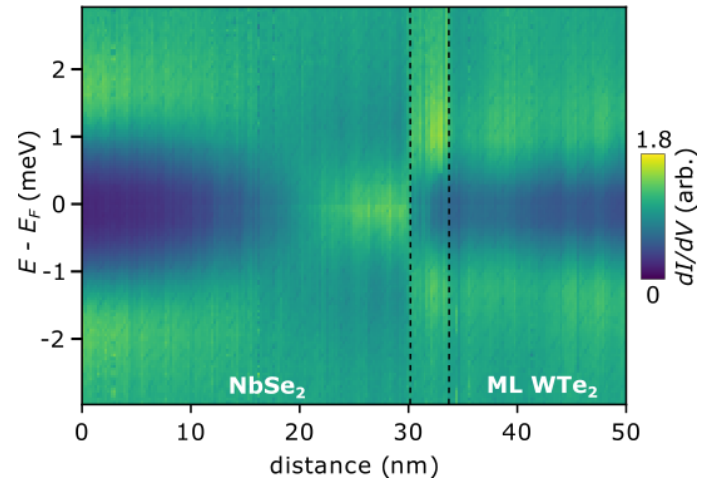
- [6] Fu, L. & Kane, C. L. Superconducting proximity effect and Majorana fermions at the surface of a topological insulator. *Phys. Rev. Lett.* **100**, 096407 (2008).
- [7] Maeno, Y., Kittaka, S., Nomura, T., Yonezawa, S. & Ishida, K. Evaluation of spin-triplet superconductivity in Sr_2RuO_4 . *J. Phys. Soc. Jpn.* **81**, 011009 (2012).
- [8] Liu, C. X., Sau, J. D., Stanescu, T. D. & Das Sarma, S. Andreev bound states versus Majorana bound states in quantum dot-nanowire-superconductor hybrid structures: Trivial versus topological zero-bias conductance peaks. *Phys. Rev. B* **96**, 075161 (2017).
- [9] Liu, C. X., Sau, J. D. & Das Sarma, S. Distinguishing topological Majorana bound states from trivial Andreev bound states: Proposed tests through differential tunneling conductance spectroscopy. *Phys. Rev. B* **97**, 214502 (2018).
- [10] Prada, E. *et al.* From Andreev to Majorana bound states in hybrid superconductor–semiconductor nanowires. *Nat. Rev. Phys.* **2**, 575–594 (2020).
- [11] Dartailh, M. C. *et al.* Missing Shapiro steps in topologically trivial Josephson junction on InAs quantum well. *Nat. Commun.* **12**, 78 (2021).
- [12] Das Sarma, S. In search of Majorana. *Nat. Phys.* **19**, 165–170 (2023).
- [13] Nadj-Perge, S. *et al.* Observation of Majorana fermions in ferromagnetic atomic chains on a superconductor. *Science* **346**, 602–607 (2014).
- [14] Jeon, S. *et al.* Distinguishing a Majorana zero mode using spin-resolved measurements. *Science* **358**, 772–776 (2017).
- [15] Kim, H. *et al.* Toward tailoring Majorana bound states in artificially constructed magnetic atom chains on elemental superconductors. *Science Advances* **4**, 5251 (2018).
- [16] Kezilebieke, S. *et al.* Topological superconductivity in a van der Waals heterostructure. *Nature* **588**, 424–428 (2020).
- [17] Hohenberg, P. C. Existence of long-range order in one and two dimensions. *Phys. Rev.* **158**, 383 (1967).
- [18] Doh, Y.-J. *et al.* Tunable supercurrent through semiconductor nanowires. *Science* **309**, 272–275 (2005).
- [19] Nadj-Perge, S. *et al.* Observation of majorana fermions in ferromagnetic atomic chains on a superconductor. *Science* **346**, 602–607 (2014).
- [20] Hart, S. *et al.* Induced superconductivity in the quantum spin Hall edge. *Nat. Phys.* **10**, 638–643 (2014).
- [21] Choi, Y.-B. *et al.* Evidence of higher-order topology in multilayer WTe_2 from Josephson coupling through anisotropic hinge states. *Nat. Mater.* **19**, 974–979 (2020).
- [22] Wang, D. *et al.* Evidence for majorana bound states in an iron-based superconductor. *Science* **362**, 333–335 (2018).
- [23] Nayak, A. K. *et al.* Evidence of topological boundary modes with topological nodal-point superconductivity. *Nat. Phys.* **17**, 1413–1419 (2021).
- [24] Li, M. *et al.* Ordered and tunable Majorana-zero-mode lattice in naturally strained LiFeAs . *Nature* **606**, 890–895 (2022).
- [25] Qian, X., Liu, J., Fu, L. & Li, J. Quantum spin Hall effect in two-dimensional transition metal dichalcogenides. *Science* **346**, 1344–1347 (2014).
- [26] Tang, S. *et al.* Quantum spin Hall state in monolayer $1T'$ – WTe_2 . *Nat. Phys.* **13**, 683 (2017).
- [27] Jia, Z.-Y. *et al.* Direct visualization of a two-dimensional topological insulator in the single-layer $1T'$ – WTe_2 . *Phys. Rev. B* **96**, 041108 (2017).
- [28] Shi, Y. *et al.* Imaging quantum spin Hall edges in monolayer WTe_2 . *Sci. Adv.* **5**, 8799 (2019).
- [29] Wu, S. *et al.* Observation of the quantum spin Hall effect up to 100 Kelvin in a monolayer crystal. *Science* **359**, 76–79 (2018).
- [30] Fatemi, V. *et al.* Electrically tunable low-density superconductivity in a monolayer topological insulator. *Science* **362**, 926 (2018).
- [31] Zhao, W. *et al.* Determination of the Spin Axis in Quantum Spin Hall Insulator Candidate Monolayer WTe_2 . *Phys. Rev. X* **11**, 041034 (2021).
- [32] Jia, J. *et al.* Tuning the many-body interactions in a helical Luttinger liquid. *Nat. Commun.* **13**, 1–7 (2022).
- [33] Lüpke, F. *et al.* Proximity-induced superconducting gap in the quantum spin Hall edge state of monolayer WTe_2 . *Nat. Phys.* **16**, 526–530 (2020).
- [34] Tao, W. *et al.* Multiband superconductivity in strongly hybridized $1T'$ – WTe_2 heterostructures. *Phys. Rev. B* **105**, 094512 (2022).
- [35] Lüpke, F. *et al.* Quantum spin hall edge states and interlayer coupling in twisted bilayer WTe_2 . *Nano Lett.* **22**, 5674–5680 (2022).
- [36] Hess, H., Robinson, R., Dynes, R., Valles Jr, J. & Waszczak, J. Scanning-tunneling-microscope observation of the Abrikosov flux lattice and the density of states near and inside a fluxoid. *Phys. Rev. Lett.* **62**, 214 (1989).
- [37] Caroli, C., De Gennes, P. & Matricon, J. Bound fermion states on a vortex line in a type II superconductor. *Phys. Lett.* **9**, 307–309 (1964).
- [38] Chen, M. *et al.* Discrete energy levels of Caroli-de Gennes-Matricon states in quantum limit in $\text{FeTe}_{0.55}\text{Se}_{0.45}$. *Nat. Comm.* **9**, 970 (2018).
- [39] Sabitova, A., Temirov, R. & Tautz, F. S. Lateral scattering potential of the $\text{PTCDA}/\text{Ag}(111)$ interface state. *Phys. Rev. B* **98**, 205429 (2018).
- [40] Martinez-Castro, J. *et al.* Disentangling the electronic structure of an adsorbed graphene nanoring by scanning tunneling microscopy. *Commun. Mater.* **3**, 57 (2022).
- [41] Sanna, A. *et al.* Real-space anisotropy of the superconducting gap in the charge-density wave material 2H-NbSe_2 . *npj Quantum Mater.* **7**, 6 (2022).
- [42] Tinkham, M. *Introduction to superconductivity* (Courier Corporation, 2004).
- [43] De Trey, P., Gygax, S. & Jan, J. P. Anisotropy of the Ginzburg-Landau parameter κ in NbSe_2 . *J. Low Temp. Phys.* **11**, 421–434 (1973).
- [44] Student. The probable error of a mean. *Biometrika* **6**, 1–25 (1908).



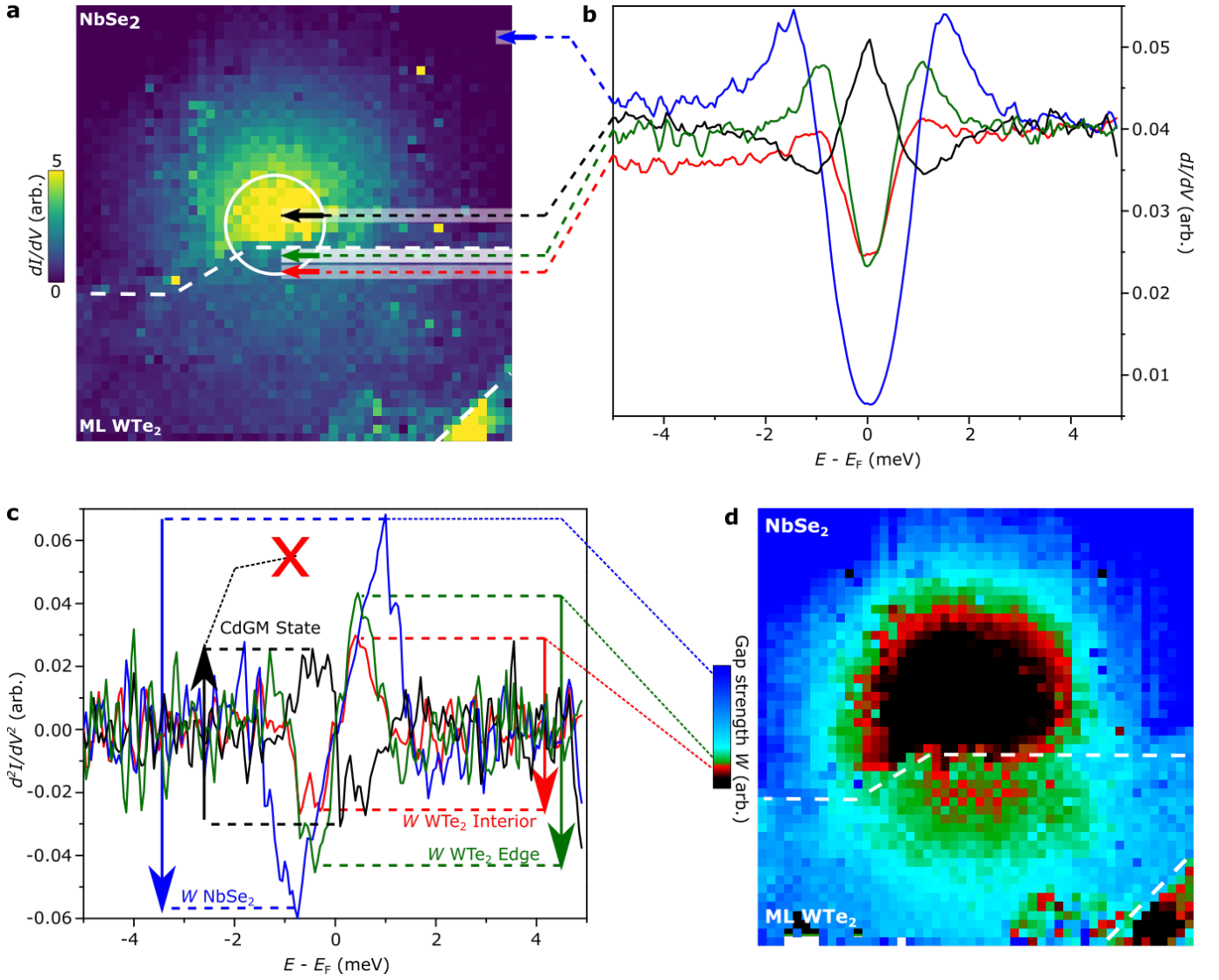
Extended Data Fig. 1. **BL WTe₂/NbSe₂ step edge.** (a) STM topography. (b) dI/dV spectral map (top) recorded along the dashed arrow in panel a and corresponding topography cross section (bottom).



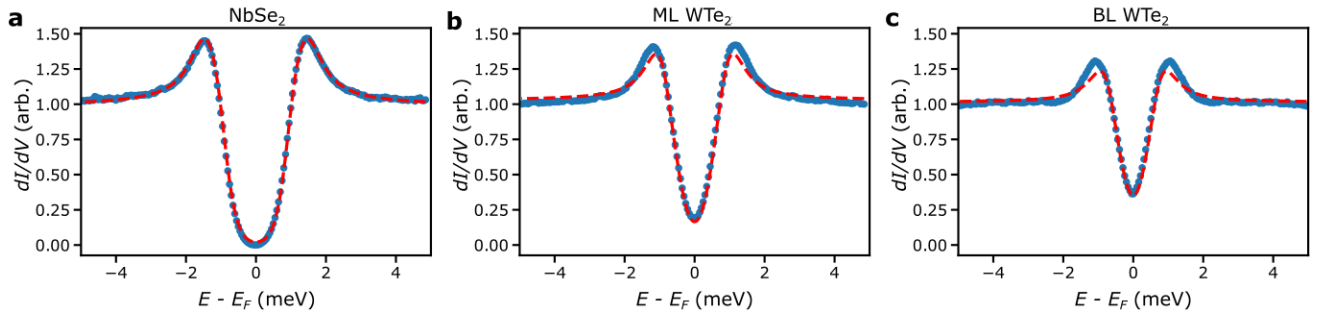
Extended Data Fig. 2. **Induced Abrikosov vortex in the interior of the ML WTe₂.** (a) dI/dV map at zero bias voltage (same as Fig. 2e), showing the vortex on the ML WTe₂. The white arrow across the vortex indicates the line along which the spectra in panel b were extracted. (b) Waterfall plot of dI/dV spectra recorded along the arrow in panel a, showing the presence of CdGM states. The vertical spacing between the curves is 0.2 (arb.).



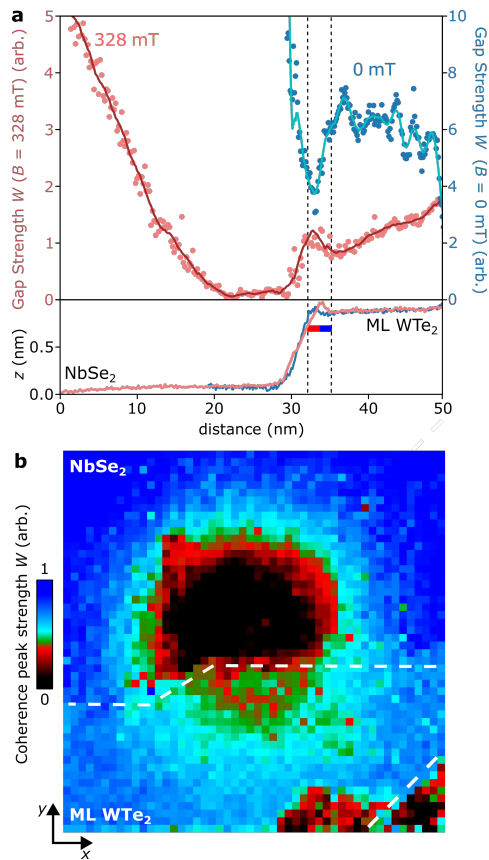
Extended Data Fig. 3. **Spectral map of ML WTe₂/ NbSe₂ with Abrikosov vortex.** High-resolution spectral map taken along the dashed arrow III in Fig. 2b, i.e., in the presence of the Abrikosov vortex. The edge state region is marked by dashed black lines (same as in Fig. 1d).



Extended Data Fig. 4. **Illustration of the FD-STs algorithm, applied to the case of the superconducting gap strength.** (a) dI/dV map at zero bias voltage (same as Fig. 2b). (b) dI/dV spectra taken at the positions indicated in panel a by black, blue, green and red arrows. (c) d^2I/dV^2 , i.e., derivative of the dI/dV spectra in panel b. The weights W assigned by the FD-STs algorithm are indicated by vertical arrows. Peaks in panel b yield $W > 0$, dips $W < 0$, corresponding to the arrow orientation. (d) Colour map of the extracted weights W , reproducing Fig. 3b.



Extended Data Fig. 5. **BCS fits to the NbSe₂, ML and BL WTe₂ spectra in Fig. 1c.** (a) The NbSe₂ fit gives an effective temperature of $T_{\text{eff}} = (2.16 \pm 0.03)$ K, gap parameters $(\Delta_1 = 1.36 \pm 0.02)$ meV, $(\Delta_2 = 1.00 \pm 0.01)$ meV and $C = 0.3 \pm 0.03$ (for details see Methods section). (b, c) The fitted WTe₂ gaps (at fixed $T_{\text{eff}} = 2.16$ K) are $\Delta_1 = (0.84 \pm 0.02)$ meV, $\Delta_2 = (0.45 \pm 0.04)$ meV, $C = 0.67 \pm 0.06$ (monolayer) and $\Delta_1 = (0.66 \pm 0.02)$ meV, $\Delta_2 = (0.25 \pm 0.06)$ meV, $C = 0.64 \pm 0.07$ (bilayer), respectively.



Extended Data Fig. 6. **Additional data plots showing the robustness of the superconducting QSH edge state.** (a) FD-STIS of the superconducting gap strength W , evaluated along a line across the ML WTe_2 / $NbSe_2$ step edge, with (red) and without (blue) vortex. Bottom panel: Corresponding topography cross section. Red and blue symbols and the vertical dashed lines indicate the location of the QSH edge state. (b) Colour map of the FD-STIS coherence peak strength W , in the same scan frame as Fig. 2a. The edges of the ML WTe_2 region are indicated by white dashed lines. Both panels, a and b, essentially reproduce the features from Fig. 3, despite analysing different quantities, i.e., the gap strength and coherence peak strength, respectively.